



# Highly active nanoporous Pt-based alloy as anode and cathode catalyst for direct methanol fuel cells



Xiaoting Chen <sup>a,1</sup>, Yingying Jiang <sup>b,1</sup>, Junzhe Sun <sup>a</sup>, Chuanhong Jin <sup>b</sup>, Zhonghua Zhang <sup>a,\*</sup>

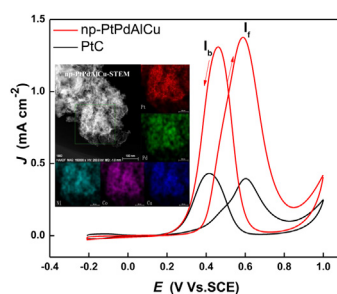
<sup>a</sup> Key Laboratory for Liquid-Solid Structural Evolution and Processing of Materials (Ministry of Education), School of Materials Science and Engineering, Shandong University, Jingshi Road 17923, Jinan 250061, PR China

<sup>b</sup> State Key Laboratory of Silicon Materials, Key Laboratory of Advanced Materials and Applications for Batteries of Zhejiang Province and Department of Materials Science and Engineering, Zhejiang University, Hangzhou, Zhejiang 310027, PR China

## HIGHLIGHTS

- Multi-component np-alloy can be fabricated by ball-milling and two-step dealloying.
- Np-PtPdAlCu alloy shows ultrafine three-dimensional ligament/channel structure.
- Np-PtPdAlCu alloy shows excellent electrocatalytic performance for DMFCs.

## GRAPHICAL ABSTRACT



## ARTICLE INFO

### Article history:

Received 6 February 2014

Received in revised form

8 May 2014

Accepted 17 May 2014

Available online 27 May 2014

### Keywords:

Direct methanol fuel cells

Electro-oxidation

Oxygen reduction reaction

Dealloying

Nanoporous alloys

## ABSTRACT

In this paper, we explore nanoporous PtPdAlCu (np-PtPdAlCu) quaternary alloy through ball-milling with the subsequent two-step dealloying strategy. The microstructure and catalytic performance of the np-PtPdAlCu catalyst have been characterized by X-ray diffraction (XRD), field-emission scanning electron microscopy (SEM), transmission electron microscopy (TEM), and electrochemical measurements. The np-PtPdAlCu catalyst exhibits an open bi-continuous interpenetrating ligament/channel structure with a length scale of  $2.3 \pm 0.5$  nm. The np-PtPdAlCu catalyst shows 2 and 3.5 times enhancement in the mass activity and area specific activity towards methanol oxidation at anode respectively, compared to the Johnson Matthey (JM) Pt/C (40 wt.%) catalyst. Moreover, the CO stripping peak of np-PtPdAlCu is 0.49 V (vs. SCE), indicating a 180 mV negative shift in comparison with the Pt/C catalyst (0.67 V vs. SCE). In addition, the np-PtPdAlCu catalyst also shows an enhanced oxygen reduction reaction (ORR) activity at cathode compared to Pt/C. The present study provides a facile and effective route to design high-performance catalysts for direct methanol fuel cells (DMFCs).

© 2014 Elsevier B.V. All rights reserved.

## 1. Introduction

Direct methanol fuel cells (DMFCs), which directly convert chemical energy of  $\text{CH}_3\text{OH}$  and  $\text{O}_2$  into electrical energy [1,2], represent a highly efficient and cost effective solution in dealing with the ever-growing worldwide energy demand. Due to their high energy density and convenient operation, DMFCs are expected to have promising applications in automotive propulsion systems

\* Corresponding author. Tel./fax: +86 531 88396978.

E-mail address: [zh\\_zhang@sdu.edu.cn](mailto:zh_zhang@sdu.edu.cn) (Z. Zhang).

<sup>1</sup> The authors equally contribute to this work.

and portable electronic devices. However, current technical problems in electrodes largely limit the extensive applications of DMFCs, such as the inferior catalytic activity in methanol oxidation reaction (MOR), being vulnerable to CO poisoning at anode, and sluggish kinetics during oxygen reduction reaction (ORR) and poor durability. In addition, the excessive use of precious metal Pt in electrode has also hampered the commercialization of DMFCs. To decrease the addition amount of Pt and enhance its utilization efficiency, one common strategy is to synthesize Pt-containing nanocatalysts through alloying Pt with other nonprecious metals or metal oxides. To date, PtRu nanorods and nanowire networks [3,4], PtCu nanotube arrays [5], PtNi nano-octahedra [6], PtSn nanorods [7], PtMo core-shell structures [8], Pt/MnO<sub>2</sub> nanohybrid [9], and Pt/TiO<sub>2</sub> particles [10] have been studied. As an alternative, researchers have sought to fabricate Pt-based multiple-component metallic alloys (e.g. PtFeCo [11], PtTiMe [12], PtRuNi [13] and PtRuCoNi [14] etc.). It has been reported that these alloys exhibit enhanced catalytic activity, durability or improved CO tolerance. Up to date, the most popular approach to get alloys is based on chemical reduction of metal salts [4,15–17]. Some researchers also explored other methods such as sol–gel process [17], solvothermal synthesis [18] and electrodeposition [19], etc. However, it should be noted that these methods are complicated and the tunability of alloy composition is limited.

Dealloying, during which an alloy is ‘parted’ by the selective dissolution of the most electrochemically active element(s) [20], has recently been attracting considerable attention to fabricate nanoporous metals/alloys. The less noble (with a smaller redox potential) element experiences corrosive dissolution and the more noble one diffuses and re-organizes, leading to the formation of a nanoporous bi-continuous structure of metal-and-void. The multiple-component metallic alloys are much more facile to be obtained through this dealloying method than other ways and can be produced in mass to meet the requirement of commercialization. To our knowledge, nanoporous metals (e.g. Cu [21,22], Pd [23], Ag [24,25], etc.) and binary alloys (e.g. PdCo [26], PdNi [27], PtAu [28,29]) have been successfully synthesized through dealloying. These nanoporous metals with large specific surface areas can greatly improve the utilization of surface active sites and have been reported with excellent sensing [30], actuation [31], and catalytic properties towards small organic molecules [20,28,32]. In addition, morphological aspects and underlying physical mechanisms of dealloying process have also aroused considerable attention [20]. To our knowledge, however, less attention has been paid to the synthesis of multiple-component nanoporous alloys through the dealloying method.

In the current paper, we fabricated an ultrafine nanoporous PtPdAlCu (np-PtPdAlCu) alloy through the combination of ball-milling with a simple two-step dealloying strategy. The obtained np-PtPdAlCu alloy was characterized with structural and electrochemical properties towards MOR and ORR. Moreover, the np-PtPdAlCu alloy shows superior catalytic activities and improved CO tolerance than the commercial Johnson Matthey (JM) Pt/C catalyst.

## 2. Experimental

The starting Al<sub>80</sub>Cu<sub>6</sub>Ni<sub>6</sub>Co<sub>6</sub>Pd<sub>1</sub>Pt<sub>1</sub> (nominal composition, at.%) alloy was prepared from pure Al, Cu, Ni, Co, Pd and Pt (99.9 wt.%) powders using a planetary ball mill machine. Stainless steel vial and balls were used, and the ball-powder mass ratio was 15:1. The rotation speed was 300 revolutions per minute and the milling time was 100 h. In order to avoid increasing of the vial temperature, the milling process was periodically interrupted every 30 min and then halted for 10 min. The dealloying of the Al<sub>80</sub>Cu<sub>6</sub>Ni<sub>6</sub>Co<sub>6</sub>Pd<sub>1</sub>Pt<sub>1</sub> alloy

powders was performed firstly in a 2 M NaOH aqueous solution for 4 h and then in a 5 M HNO<sub>3</sub> solution for 4 h at room temperature. Finally, the samples were rinsed in distilled water and dehydrated alcohol for several times.

X-ray diffractograms of the mechanically alloyed Al<sub>80</sub>Cu<sub>6</sub>Ni<sub>6</sub>Co<sub>6</sub>Pd<sub>1</sub>Pt<sub>1</sub> precursor and as-dealloyed samples were obtained by an X-ray diffractometer (XRD, Rigaku D/max-rB) with Cu K $\alpha$  radiation. The microstructure of the as-dealloyed catalyst was characterized using a scanning electron microscope (SEM, Quanta FEG 250) and a high-resolution transmission electron microscope (HRTEM, FEI Tecnai G2). The fast Fourier transform (FFT) patterns were obtained from the corresponding HRTEM images using a software named Gatan Digital Micrograph. The chemical compositions of the as-dealloyed samples were determined by an energy-dispersive X-ray (EDX) analyzer attached to SEM. In addition, scanning transmission electron microscopy (STEM) images and elemental mapping were obtained with an FEI-TITAN ChemiSTEM with a Bruker Super-X EDX detectors at 200 kV.

All electrochemical measurements were carried out in a standard three-electrode cell with a CHI 760E Potentiostat. The side arms contained a saturated calomel electrode (SCE) reference electrode and a bright Pt plate counter electrode. The catalyst ink was prepared as follows: 2.0 mg of the synthesized alloy, 3.0 mg XC-72 carbon powder, 1.5 mL isopropanol and 0.5 mL Nafion solution (0.5 wt.%) were ultrasonically mixed for 30 min. Afterward, 4  $\mu$ L homogeneously mixed catalyst suspension was dropped on a freshly polished glassy carbon (GC) electrode with a diameter of 4 mm (apparent surface area 0.126 cm<sup>2</sup>) and then dried in a vacuum tank at room temperature for at least 3 h. The coated GC electrode was used as the working electrode. The cyclic voltammetry (CV) behavior of the catalyst was determined in a 0.5 M H<sub>2</sub>SO<sub>4</sub> solution deaerated with N<sub>2</sub>. Several scans were performed until reproducible voltammograms were obtained. The electrocatalytic activity of the as-prepared catalyst for the methanol oxidation was characterized in a N<sub>2</sub>-purged 0.5 M H<sub>2</sub>SO<sub>4</sub> + 0.5 M CH<sub>3</sub>OH solution at 30 °C. The CO tolerance was characterized by CO stripping firstly maintaining the working electrode in the 0.5 M H<sub>2</sub>SO<sub>4</sub> solution saturated with bubbling CO gas for the period of 500 s. After CO adsorption, the electrode was transferred into a CO-free 0.5 M H<sub>2</sub>SO<sub>4</sub> solution followed by potential scanning between –0.21 V and 1.06 V (vs. SCE).

In the cathode scanning, a rotating disk electrode (RDE) technique was employed to electrochemically evaluate the ORR process of the catalyst. A reversible hydrogen electrode (RHE) and a rotating disk electrode with a diameter of 5 mm (geometric surface area 0.196 cm<sup>2</sup>) were used as the reference and working electrode, respectively. The electrochemical properties of the catalyst in a N<sub>2</sub>-saturated 0.1 M HClO<sub>4</sub> were first studied by cyclic voltammetry to obtain a stable cyclic voltammogram in order to determine the electrochemically active surface area (ECSA) of the Pt catalyst. Then, the ORR experiment was performed under a rotation speed of 1600 rpm at a scan rate of 10 mV s<sup>–1</sup>. Saturation with high purity oxygen was performed prior to the electrocatalytic activity measurement. We benchmarked the electrochemical properties of the np-PtPdAlCu against the Pt/C commercial catalyst under the identical experimental conditions.

## 3. Results and discussion

### 3.1. Microstructural characterization of np-PtPdAlCu

According to the XRD results (Fig. S1), elemental peaks disappear after milling of 100 h, indicating the alloying of the constitutional elements. The mechanically alloyed Al<sub>80</sub>Cu<sub>6</sub>Ni<sub>6</sub>Co<sub>6</sub>Pd<sub>1</sub>Pt<sub>1</sub> precursor mainly consists of an Al<sub>4</sub>Cu<sub>9</sub>-type (PDF No. 65-3347)

intermetallic phase. In addition, there exist some peaks on the XRD pattern, which cannot be identified by any known phase (Fig. S1). By comparison with the reference profile of  $\text{Al}_4\text{Cu}_9$ , it is reasonable to assume that the minor Pt and Pd exist in the  $\text{Al}_4\text{Cu}_9$  phase. After dealloying in the NaOH and  $\text{HNO}_3$  solutions, the XRD pattern illustrates four main Bragg peaks located at scattering angles of ca. 39.8, 46.2, 67.6 and 81.8, as shown in Fig. 1. These diffraction peaks correspond to a face centered cubic (f.c.c.) Pt phase (PDF No. 04-0802). It has been reported that incorporation of other metal elements leads to the shifting of Pt peaks compared to pure Pt [33]. Here no obvious shifting of Pt peaks can be discerned on the XRD pattern (Fig. 1).

Fig. 2a shows the SEM image of the as-dealloyed powders. It is clear that the powders contain a plenty of irregular particles with an almost homogeneous size distribution. Most of the particles are smaller than 1  $\mu\text{m}$ . However, it should be noted that the nanoporous structure of the as-dealloyed powders cannot be well distinguished by SEM even at higher magnification, as shown in Fig. 2b. A typical EDX spectrum (Fig. S2) reveals that the as-dealloyed sample is mainly composed of Pt (72.6 at.%), Pd (11.7 at.%), Al (8.5 at.%) and Cu (7.2 at.%). Only trace Ni and Co can be detected in the as-dealloyed sample by EDX (Fig. S2). Due to the single-phase nature of the as-dealloyed sample (Fig. 1), it is reasonable to assume that Pd, Al and Cu exist in the Pt phase in the form of solid solution. According to the EDX results, the as-dealloyed samples can be designated as np-PtPdAlCu for simplicity.

Fig. 3 shows the TEM and HRTEM images of the np-PtPdAlCu alloy fabricated by dealloying the as-milled  $\text{Al}_{80}\text{Cu}_6\text{Ni}_6\text{Co}_6\text{Pd}_1\text{Pt}_1$  powders in the NaOH and  $\text{HNO}_3$  solutions. Obviously, the np-PtPdAlCu particles show a typical bi-continuous ligament/channel structure and the characteristic length scale of ligament/channel is only  $2.3 \pm 0.5$  nm (Fig. 3a). The corresponding SAED pattern is given in the inset of Fig. 3a, which consists of diffraction rings indicating the nanocrystalline nature of the selected area. The SAED pattern can be indexed as (111), (200), (220) and (311) reflections of f.c.c. Pt, and is in agreement with the XRD results shown in Fig. 1. The HRTEM image further confirms the ultrafine nanoporous structure of the np-PtPdAlCu alloy (Fig. 3b). Furthermore, typical lattice fringes can be clearly observed in the HRTEM image and the corresponding FFT pattern is shown in the inset of the image. The FFT

pattern also verifies the nanocrystalline nature of the connected ligaments. The lattice spacing of one nanocrystal was calculated to be 0.223 nm (as indicated in Fig. 3b), which is close to the value (0.226 nm) of the (111) crystal plane of pure Pt. Some TEM and HRTEM images are also presented in Fig. S3 and further confirm the ultrafine nanoporous structure of the np-PtPdAlCu alloy.

To gain further insight into the elemental distribution in the np-PtPdAlCu alloy, we carried out elemental analysis by STEM and EDX mapping. Fig. 4a shows a STEM micrograph of the np-PtPdAlCu alloy, which clearly shows the z-contrast nanoporous structure. One area is highlighted by a green (in the web version) rectangle in Fig. 4a for elemental mapping. The elemental mapping spectra are presented in Fig. 4b–f. It can be seen from Fig. 4b–f that the spatial distribution of Pt, Pd, Cu, Co and Ni elements is completely overlapped and without much agglomeration. At least three areas were analyzed by EDX mapping and the average values were obtained. The contents of Pd, Cu, Ni and Co are 13.1 at.%, 4.9 at.%, 0.3 at.% and 0.9 at.% respectively, which are consistent with the EDX results obtained by SEM-EDX (Fig. S2).

On the basis of the above results, it can be concluded that the np-PtPdAlCu alloy can be fabricated by mechanical alloying and subsequent two-step dealloying. The dealloying-induced formation of the np-PtPdAlCu alloy can be addressed as follows. It is known that the dealloying process involves the selective dissolution of the less noble element and the diffusion/self-organization of the more noble element along the alloy/solution interface [20]. When dealloying in the NaOH solution, most of Al is preferentially etched away (to form  $\text{AlO}_2^-$ ) and other elements (Pt, Pd, Cu, Ni and Co) retain in the as-dealloyed samples. The following dealloying in the  $\text{HNO}_3$  solution leads to partial dissolution of Cu, Al and Pd. Unexpectedly, almost all the Ni and Co are dissolved (the residue of less than 1.0 at.%) after the second dealloying in the  $\text{HNO}_3$  solution. It should be noted that the Al always remained after similar corrosion steps [34–36]. Moreover, the residual element cannot be completely removed but asymptotically reaches a limit even at exhaustively long etching times (up to 100 h) [37]. At the same time, the more noble Pt atoms diffuse and re-organize into the ultrafine nanoporous structure. And the residual Pd, Cu and Al exist in the Pt lattice in the form of solid solution.

### 3.2. Catalytic activity of np-PtPdAlCu towards methanol oxidation

The np-PtPdAlCu alloy and commercial JM Pt/C (40 wt.%) catalyst were characterized in the 0.5 M  $\text{H}_2\text{SO}_4$  solution by cyclic voltammetry in order to investigate their electrocatalytic activity for MOR. The stabilized cyclic voltammetry curves (CVs) of the np-PtPdAlCu and commercial JM Pt/C (40 wt.%) catalyst are overlaid in Fig. 5a. Basically, the np-PtPdAlCu alloy and Pt/C catalyst exhibit similar CV features including (i) the adsorption–desorption of hydrogen, (ii) the double electric layer formation and (iii) the Pt oxidation and reduction of Pt oxides (Fig. 5a). In comparison, there still exists difference between the CV features of the np-PtPdAlCu alloy and Pt/C catalyst. Firstly, the broader double electric layer and featureless shoulder region from  $-0.20$  to  $0.20$  V (vs. SCE) develop on np-PtPdAlCu, which are comparable to those reported in the literature [33,38–40]. These can be caused by the addition of other alloying elements, especially Pd and Cu [39]. Moreover, as indicated by dotted line in Fig. 5a, the peak position for the reduction of Pt oxides shifts to the positive direction compared to the Pt/C catalyst in the back scan, possibly due to the contribution of other alloying elements [40]. The ECSA of a catalyst containing Pt is calculated according to the following equation  $\text{ECSA}_{\text{Pt}}(\text{m}^2 \text{g}^{-1}) = Q_{\text{H}}/(2.1 \times m_{\text{Pt}})$  (where  $Q_{\text{H}}$  (C) is the charge exchanged during hydrogen desorption on the surface, and  $m_{\text{Pt}}$  (g) is the amount of Pt loaded on the electrode) [41]. However, Pd also

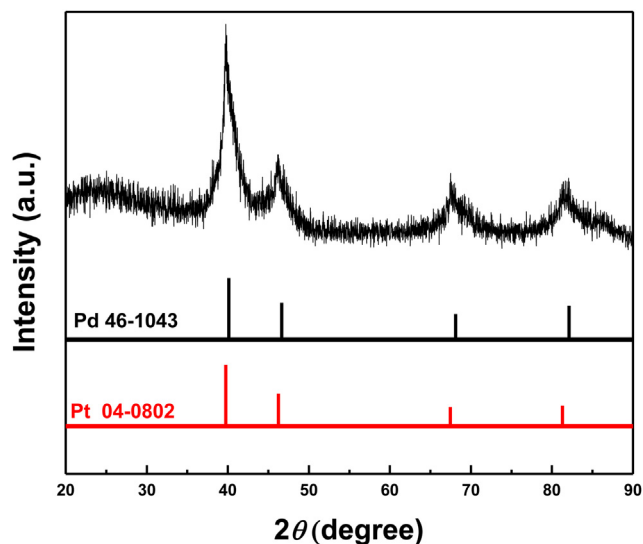
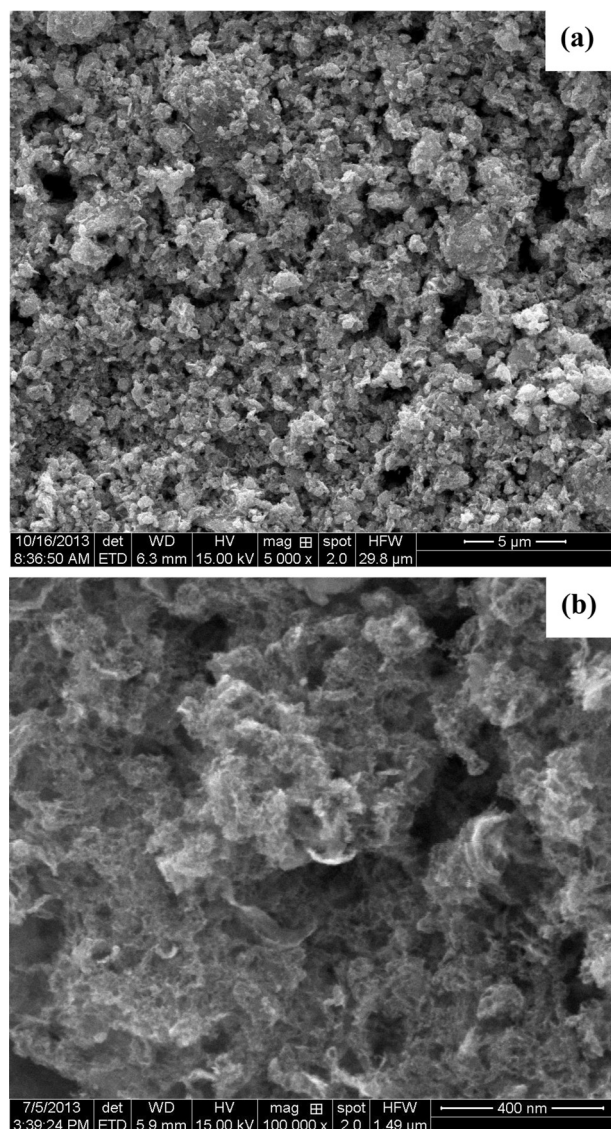


Fig. 1. XRD pattern of the as-dealloyed samples obtained by dealloying the mechanically alloyed  $\text{Al}_{80}\text{Cu}_6\text{Ni}_6\text{Co}_6\text{Pd}_1\text{Pt}_1$  powders firstly in the 2 M NaOH solution and then in the 5 M  $\text{HNO}_3$  solution at room temperature.



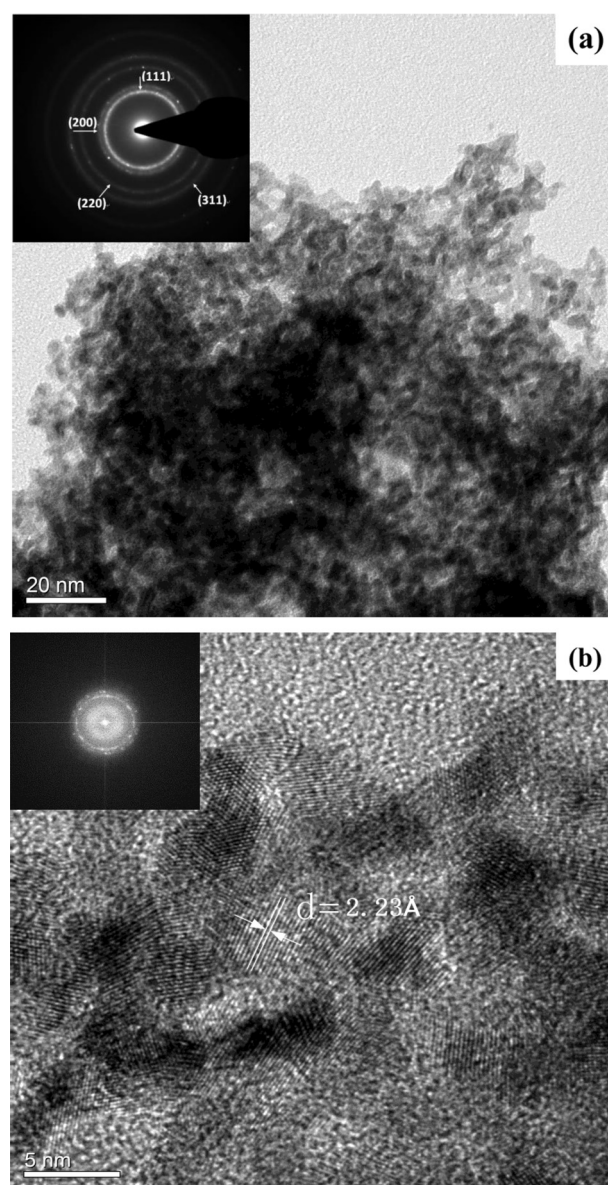


**Fig. 2.** SEM images showing the microstructure of the as-dealloyed samples obtained by the two-step dealloying method.

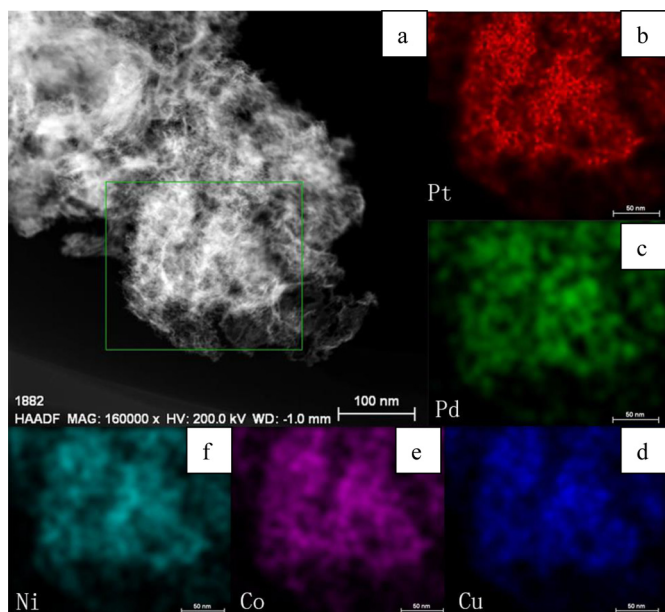
belongs to  $H_2$  absorption materials and the CO stripping method has also been used as an effective route to evaluate the ECSA of Pd or Pd-based electrocatalysts [42–44]. Interestingly, the value of  $26 \text{ m}^2 \text{ g}^{-1}$  obtained from CO stripping peak is consistent with the value ( $25 \text{ m}^2 \text{ g}^{-1}$ ) determined from the above equation for the present np-PtPdAlCu catalyst. Thus the value of  $25 \text{ m}^2 \text{ g}^{-1}$  was used for np-PtPdAlCu in the following evaluation of catalytic activity. In addition, the ECSA of the commercial Pt/C catalyst was determined to be  $47 \text{ m}^2 \text{ g}^{-1}$ . Due to the alloy surface, many researchers have reported lower ECSA of the Pt-based alloy nanostructures [28,40]. Additionally, Fig. S4 shows the initial CV cycles of the np-PtPdAlCu alloy in the  $0.5 \text{ M H}_2\text{SO}_4$  solution. It can be observed that the CVs of the np-PtPdAlCu alloy gradually show well-separated hydrogen regions in the low potential region with increasing CV cycles, as highlighted by an upward arrow in Fig. S4. Moreover, the reduction potential of the Pt oxides forming in the positive scan shifts slightly to the positive position with increase of the cycles (Fig. S4). In general, conducting potential cycling can induce the leaching of the less-noble metal(s) and result in a PtPd- or Pt-rich skin structure for typical multi-metallic nanoparticle catalysts [45–48]. The

voltammetric leaching phenomenon proves to the formation of a stable highly active catalyst. Therefore, these variations in CVs are attributed to the irreversible dissolution (highlighted by one downward arrow in Fig. S4) of minor Pd, Cu and Al from the ligament surface of the np-PtPdAlCu catalyst, which gradually forms a stable Pt-rich alloy layer.

The np-PtPdAlCu catalyst exhibits significantly enhanced electrocatalytic activity towards methanol oxidation (Fig. 5). Fig. 5b and c shows the ECSA- and Pt mass-normalized CVs for the np-PtPdAlCu alloy and Pt/C catalyst in the  $0.5 \text{ M H}_2\text{SO}_4 + 0.5 \text{ M CH}_3\text{OH}$  solution, respectively. It can be seen that the peak potential is  $0.59 \text{ V}$  (vs. SCE) in the forward scan for the np-PtPdAlCu, which is slightly lower than that ( $0.60 \text{ V}$  vs. SCE) of Pt/C. Moreover, the onset potentials are comparable for both catalysts. The current densities in the forward scan are normally utilized to assess the electrocatalytic activity of catalysts. As shown in Fig. 5b, the specific activity (in the forward scan) of the np-PtPdAlCu is  $1.4 \text{ mA cm}^{-2}$ , which is 3.5 times that of the Pt/C catalyst ( $0.4 \text{ mA cm}^{-2}$ ). As to the



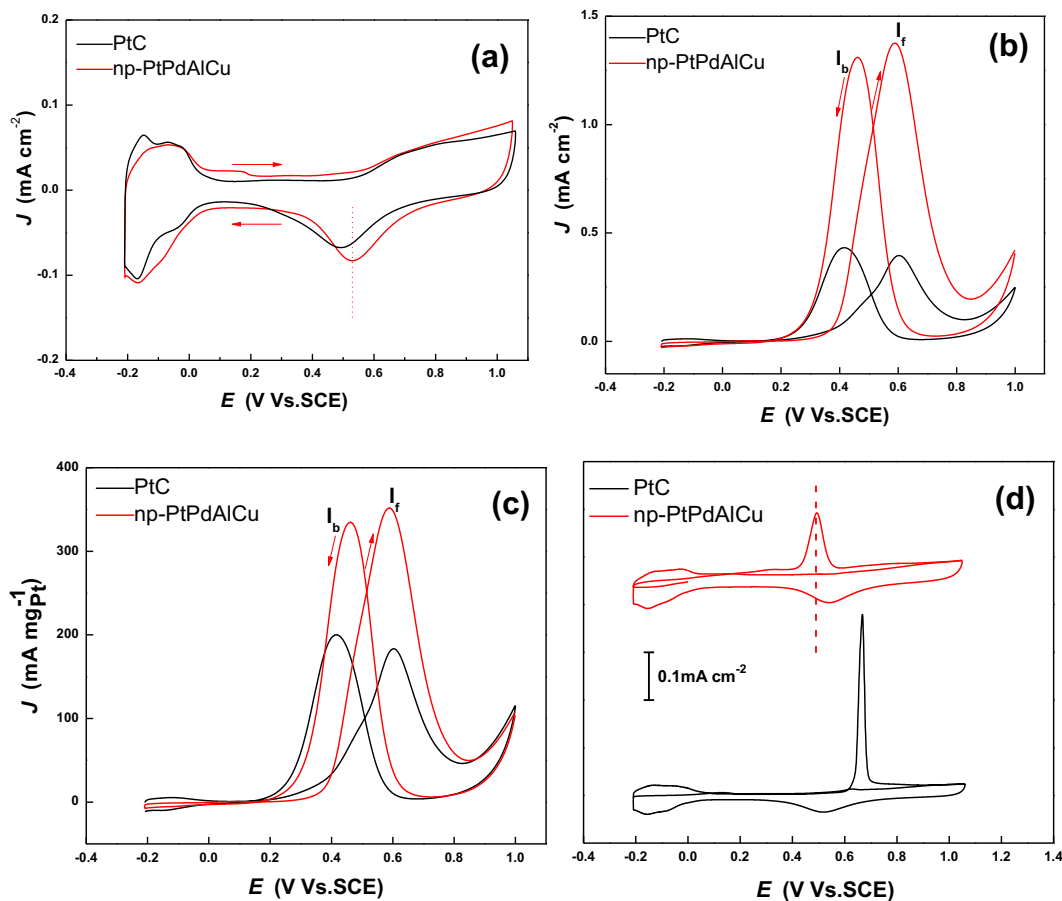
**Fig. 3.** (a) TEM and (b) HRTEM images showing the nanoporous microstructure of the np-PtPdAlCu alloy fabricated by the two-step dealloying method. Insets in (a, b): corresponding SAED and FFT patterns, respectively.



**Fig. 4.** (a) STEM image showing the microstructure of the np-PtPdAlCu alloy fabricated by the two-step dealloying method. (b–f) EDX mapping images corresponding to the marked area in (a).

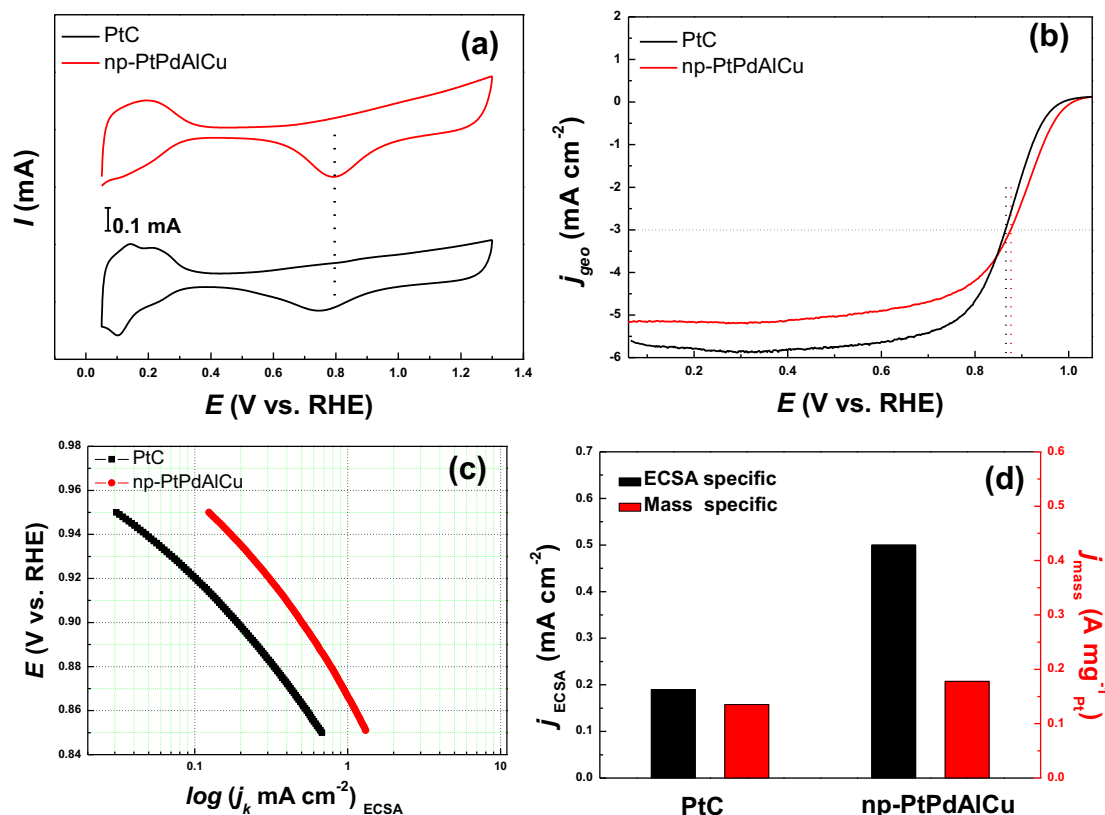
mass-normalized current densities (Fig. 5c), the np-PtPdAlCu catalyst shows the highest MOR activity of  $360.8 \text{ mA mg}_{\text{Pt}}^{-1}$ , which is about 2 times of that for Pt/C ( $183 \text{ mA mg}_{\text{Pt}}^{-1}$ ). Since Mancharan and Goodenough [49] have discussed the catalysis mechanism of the MOR on platinum, the empirical criterion of  $I_{\text{forward}}/I_{\text{backward}}$  ( $I_f/I_b$ ) is normally used to describe the tolerance of the catalyst to accumulation of carbonaceous species by many researchers [38,50,51]. A low  $I_f/I_b$  ratio indicates poor oxidation of methanol during the forward scan and excessive accumulation of carbonaceous residues on the catalyst surface, while a high  $I_f/I_b$  ratio shows the converse case. In our experiments, the np-PtPdAlCu alloy shows a larger  $I_f/I_b$  ratio of  $\sim 1.1$  compared to that ( $I_f/I_b$ :  $\sim 0.9$ ) of the Pt/C catalyst. However, there exist controversies over the use of  $I_f/I_b$  to evaluate the CO tolerance of Pt-based electrocatalysts. Most recently, Hofstead-Duffy et al. [52] have argued that the use of the  $I_f/I_b$  empirical criterion is inappropriate by a series of experiments. Thus, the subsequent CO stripping experiment was carried out to provide better measurement of CO tolerance of our np-PtPdAlCu catalyst.

Fig. 5d shows the CO stripping curves of the np-PtPdAlCu and Pt/C catalyst. For the np-PtPdAlCu catalyst, the CO stripping curve shows a sharp peak at 0.49 V (vs. SCE), which is much more negative (about 180 mV) than that of the Pt/C catalyst (0.67 V vs. SCE). The lower potential for CO electrooxidation indicates that the CO adsorption is much weaker on np-PtPdAlCu, implying the enhanced CO-tolerance of Pt by alloying with Pd, Al and Cu. The anode reaction at direct methanol fuel cells performs as  $\text{CH}_3\text{OH} + \text{H}_2\text{O} \rightarrow \text{CO}_2 + 6\text{H} + 6\text{e}^-$  [53]. Although the oxidation of



**Fig. 5.** (a) CVs of the np-PtPdAlCu and Pt/C catalysts in the  $\text{N}_2$  purged  $0.5 \text{ M H}_2\text{SO}_4$  solution. (Scan rate:  $50 \text{ mV s}^{-1}$ ) (b) ECSA-normalized (c) mass-normalized CVs for methanol electro-oxidation in the  $0.5 \text{ M H}_2\text{SO}_4 + 0.5 \text{ M CH}_3\text{OH}$  solution at  $30^\circ\text{C}$ , and (d) electrochemical CO-stripping curves in the  $0.5 \text{ M H}_2\text{SO}_4$  solution. (Scan rate:  $20 \text{ mV s}^{-1}$ ).





**Fig. 6.** (a) CV curves of the np-PtPdAlCu and Pt/C catalysts in the N<sub>2</sub>-purged 0.1 M HClO<sub>4</sub> solution. (Scan rate: 50 mV s<sup>-1</sup>) (b) ORR polarization curves for the np-PtPdAlCu and Pt/C catalysts in the O<sub>2</sub>-saturated 0.1 M HClO<sub>4</sub> solution at 30 °C at 1600 rpm. (Scan rate: 10 mV s<sup>-1</sup>) (c) ECSA-normalized specific kinetic current densities ( $j_k$ ) for the np-PtPdAlCu and Pt/C catalysts. (d) The ECSA- and mass-normalized specific kinetic current densities for the np-PtPdAlCu and Pt/C catalysts at 0.90 V (vs. RHE).

methanol is rapid on clean Pt, CO appears as an intermediate in the reaction and poisons the catalyst surface. The turnover of catalytic sites involves oxidation of CO to CO<sub>2</sub>, using oxygen-containing species (mainly OH) supplied by water. However, the adsorption of H<sub>2</sub>O on Pt requires a high overpotential [17]. Therefore, the superior performance of the obtained catalysts relative to Pt/C possibly ascribes to three effects. (i) The oxophilic metal (Pd, Al and Cu) is thought to provide active sites, or the sites of a single Pt atom surrounded by these atoms favor for water adsorption and also allow the transportation of the poisoning species from the Pt sites during the reaction [17], (ii) In the ligand-effect or electronic model, the role of alloying elements is to modify the electronic structure/properties of Pt by contributing to d-electron density [54]. The role of ensemble elements has been put on abundant research for binary alloys [16,55–57], while the distinctive mechanism between Pt and each element in the multicomponent catalyst remains to be investigated. (iii) The unique open bicontinuous ligament-channel structure can facilitate the diffusion of involved species in the electrolyte and conduce to the electrical transfer.

### 3.3. The ORR performance of np-PtPdAlCu

Fig. 6a presents the CV of the np-PtPdAlCu electrocatalyst in the N<sub>2</sub>-saturated 0.1 M HClO<sub>4</sub> solution. For comparison, the CV is superposed with the signal from the Pt/C catalyst. The Pt/C and np-PtPdAlCu catalysts both display typical features which should be shown in perchloric media. In contrast, the peak position for the reduction of Pt oxides in the back scan of the np-PtPdAlCu catalyst shows a positive shift, indicating earlier onset of Pt–O(H) reduction [58]. These results also agree with our experiments at anode, and further reveal the nanoporous alloy structure

of np-PtPdAlCu. The ECSAs of the np-PtPdAlCu and Pt/C catalysts were determined according to CVs in Fig. 6a. Fig. 6b shows the steady state polarization curves for the ORR catalyzed by the np-PtPdAlCu and Pt/C at 30 °C and 10 mV s<sup>-1</sup>. According to the potential, the polarization curves for the ORR are divided into three regions: a mass-transfer-controlled region (below 0.8 V vs. RHE), the mixed region (between 0.8 and 1.0 V vs. RHE), and kinetics-controlled region (above 1.0 V vs. RHE) [54]. The np-PtPdAlCu alloy exhibits higher half-wave potential at 0.88 V (vs. RHE), which is 20 mV more positive than that of the Pt/C catalyst (0.86 V vs. RHE), implying the improved reaction kinetics for ORR at lower overpotential. Fig. 6c also shows the ECSA-normalized specific kinetic current densities, and the np-PtPdAlCu alloy exhibits higher specific activity than that of the Pt/C catalyst in the whole potential range (0.85–0.95 V vs. RHE). ORR currents at 0.90 V vs. RHE, which are in the range of an electro-transfer-limited process at the cathode, are usually used to evaluate the catalytic activity for the ORR [59–61]. As shown in Fig. 6d, the Pt/C catalyst has a mass activity of 135 mA mg<sub>Pt</sub><sup>-1</sup> and a specific activity of 0.2 mA cm<sup>-2</sup>. In contrast, the np-PtPdAlCu catalyst has a mass activity of 177 mA mg<sub>Pt</sub><sup>-1</sup> and a specific activity of 0.5 mA cm<sup>-2</sup>, which are ~1.3 and 2.5 times those of the commercial Pt/C catalyst. In an acidic solution, O<sub>2</sub> can be reduced in a 4e<sup>-</sup> process and converted into H<sub>2</sub>O: O<sub>2</sub> + 4H<sup>+</sup> + 4e<sup>-</sup> → 2H<sub>2</sub>O [2,62–64]. In this mechanism, O–O is cleaved to form OH<sub>ads</sub> species [2,64]. By using multiple-component alloy, the d-band center of Pt shifts due to a strain effect (caused by the lattice mismatch), which lowers the adsorption energy of surface [2,63]. On the other hand, the three-dimensional bi-continuous nanoporosity with interconnected channels and nano-sized ligaments provides excellent transport paths for all involved ions, molecules and electrons [55].

#### 4. Conclusions

In summary, a novel np-PtPdAlCu catalyst has been fabricated through the combination of ball-milling following with a simple two-step dealloying. The np-PtPdAlCu catalyst exhibits a three-dimensional bicontinuous ligament/channel structure with the length scale of  $2.3 \pm 0.5$  nm. The np-PtPdAlCu alloy reveals a superior electrocatalytic activity and CO tolerance towards electro-oxidation of methanol at anode in an acidic circumstance. Moreover, the catalyst also shows improved activity when applied to oxygen reduction at cathode compared to the commercial Pt/C catalyst. The present strategy is more facile to design various multiple-component metallic alloy electrocatalysts than other ways, and the nanoporous alloy catalysts can be produced in mass to meet the requirement of commercialization (Fig. S5).

#### Acknowledgments

The authors gratefully acknowledge financial support by National Natural Science Foundation of China (51371106), National Basic Research Program of China (973, 2012CB932800), Program for New Century Excellent Talents in University (MOE, NCET-11-0318), and Specialized Research Fund for the Doctoral Program of Higher Education of China (20120131110017). In addition, the work on STEM-EDX mapping was carried out in the Centre of Electron Microscopy of Zhejiang University.

#### Appendix A. Supplementary data

Supplementary data related to this article can be found at <http://dx.doi.org/10.1016/j.jpowsour.2014.05.089>.

#### References

- [1] G.S. Chai, J.S. Yu, *J. Mater. Chem.* 19 (2009) 6842–6848.
- [2] J.N. Tiwari, R.N. Tiwari, G. Singh, K.S. Kim, *Nano Energy* 2 (2013) 553–578.
- [3] S.J. Yoo, T.Y. Jeon, K.S. Kim, T.-H. Lim, Y.-E. Sung, *Phys. Chem. Chem. Phys.* 12 (2010) 15240–15246.
- [4] B. Li, D.C. Higgins, S. Zhu, H. Li, H. Wang, J. Ma, Z. Chen, *Catal. Commun.* 18 (2012) 51–54.
- [5] X. Zhang, D. Li, D. Dong, H. Wang, P.A. Webley, *Mater. Lett.* 64 (2010) 1169–1172.
- [6] C. Cui, L. Gan, M. Heggen, S. Rudi, P. Strasser, *Nat. Mater.* 12 (2013) 765–771.
- [7] S. Sun, G. Zhang, D. Geng, Y. Chen, M.N. Banis, R. Li, M. Cai, X. Sun, *Chem. Eur. J.* 16 (2010) 829–835.
- [8] O. Guillén-Villafuerte, R. Guil-López, E. Nieto, G. García, J.L. Rodríguez, E. Pastor, J.L.G. Fierro, *Int. J. Hydrogen Energy* 37 (2012) 7171–7179.
- [9] H. Huang, Q. Chen, M. He, X. Sun, X. Wang, *J. Power Sources* 239 (2013) 189–195.
- [10] L. Xiong, A. Manthiram, *Electrochim. Acta* 49 (2004) 4163–4170.
- [11] S. Kim, C. Kim, H. Lee, *Top. Catal.* 53 (2010) 686–693.
- [12] T. He, E. Kreidler, *Phys. Chem. Chem. Phys.* 10 (2008) 3731–3738.
- [13] Z.B. Wang, C.R. Zhao, P.F. Shi, Y.S. Yang, Z.B. Yu, W.K. Wang, G.P. Yin, *J. Phys. Chem. C* 114 (2009) 672–677.
- [14] M.V. Martínez-Huerta, S. Rojas, J.L. Gómez de la Fuente, P. Terreros, M.A. Peña, J.L.G. Fierro, *Appl. Catal. B* 69 (2006) 75–84.
- [15] S.F. Zheng, J.S. Hu, L.S. Zhong, L.J. Wan, W.G. Song, *J. Phys. Chem. C* 111 (2007) 11174–11179.
- [16] G. Selvarani, S.V. Selvaganes, S. Krishnamurthy, G.V.M. Kiruthika, P. Sridhar, S. Pitchumani, A.K. Shukla, *J. Phys. Chem. C* 113 (2009) 7461–7468.
- [17] K.I.B. Eguiluz, G.R.P. Malpass, M.M.S. Pupo, G.R. Salazar-Banda, L.A. Avaca, *Energy Fuels* 24 (2010) 4012–4024.
- [18] A. Sarkar, A. Vadivel Murugan, A. Manthiram, *Fuel Cells* 10 (2010) 375–383.
- [19] L. Liu, Z. Huang, D. Wang, R. Scholz, E. Pippel, *Nanotechnology* 22 (2011) 105604.
- [20] J. Erlebacher, M.J. Aziz, A. Karma, N. Dimitrov, K. Sieradzki, *Nature* 410 (2001) 450–453.
- [21] Y. Wang, Y. Wang, C. Zhang, T. Kou, Z. Zhang, *CrystEngComm* 14 (2012) 8352–8356.
- [22] Z. Qi, C. Zhao, X. Wang, J. Lin, W. Shao, Z. Zhang, X. Bian, *J. Phys. Chem. C* 113 (2009) 6694–6698.
- [23] X. Wang, W. Wang, Z. Qi, C. Zhao, H. Ji, Z. Zhang, *Int. J. Hydrogen Energy* 37 (2012) 2579–2587.
- [24] H. Qiu, Z. Zhang, X. Huang, Y. Qu, *ChemPhysChem* 12 (2011) 2118–2123.
- [25] C. Zhang, J. Sun, J. Xu, X. Wang, H. Ji, C. Zhao, Z. Zhang, *Electrochim. Acta* 63 (2012) 302–311.
- [26] M. Hakamada, M. Mabuchi, *J. Alloys Compd.* 479 (2009) 326–329.
- [27] Z. Qi, H. Geng, X. Wang, C. Zhao, H. Ji, C. Zhang, J. Xu, Z. Zhang, *J. Power Sources* 196 (2011) 5823–5828.
- [28] Z. Zhang, Y. Wang, X. Wang, *Nanoscale* 3 (2011) 1663–1674.
- [29] J. Zhang, H. Ma, D. Zhang, P. Liu, F. Tian, Y. Ding, *Phys. Chem. Chem. Phys.* 10 (2008) 3250–3255.
- [30] T. You, O. Niwa, M. Tomita, S. Hirono, *Anal. Chem.* 75 (2003) 2080–2085.
- [31] J. Weissmüller, R.N. Viswanath, D. Kramer, P. Zimmer, R. Würschum, H. Gleiter, *Science* 300 (2003) 312–315.
- [32] H. Ji, J. Frenzel, Z. Qi, X. Wang, C. Zhao, Z. Zhang, G. Eggeler, *CrystEngComm* 12 (2010) 4059–4062.
- [33] M. Ammam, E.B. Easton, *J. Power Sources* 215 (2012) 188–198.
- [34] X. Wang, J. Sun, C. Zhang, T. Kou, Z. Zhang, *J. Phys. Chem. C* 116 (2012) 13271–13280.
- [35] Z. Zhang, C. Zhang, J. Sun, T. Kou, Q. Bai, Y. Wang, Y. Ding, *J. Mater. Chem. A* 1 (2013) 3620–3628.
- [36] C. Xu, Q. Li, Y. Liu, J. Wang, H. Geng, *Langmuir* 28 (2011) 1886–1892.
- [37] K. Sieradzki, R.R. Corderman, K. Shukla, R.C. Newman, *Philos. Mag. A* 59 (1989) 713–746.
- [38] Y.-W. Lee, A.R. Ko, S.-B. Han, H.-S. Kim, K.-W. Park, *Phys. Chem. Chem. Phys.* 13 (2011) 5569–5572.
- [39] H.H. Li, C.H. Cui, S. Zhao, H.B. Yao, M.R. Gao, F.J. Fan, S.H. Yu, *Adv. Energy Mater.* 2 (2012) 1182–1187.
- [40] C. Xu, J. Hou, X. Pang, X. Li, M. Zhu, B. Tang, *Int. J. Hydrogen Energy* 37 (2012) 10489–10498.
- [41] C. He, Y. Liang, R. Fu, D. Wu, S. Song, R. Cai, *J. Mater. Chem.* 21 (2011) 16357–16364.
- [42] X. Wang, W. Wang, Z. Qi, C. Zhao, H. Ji, Z. Zhang, *J. Power Sources* 195 (2010) 6740–6747.
- [43] X. Wang, Y. Tang, Y. Gao, T. Lu, *J. Power Sources* 175 (2008) 784–788.
- [44] Y. Huang, X. Zhou, J. Liao, C. Liu, T. Lu, W. Xing, *Electrochim. Commun.* 10 (2008) 621–624.
- [45] C.H. Cui, S.H. Yu, *Acc. Chem. Res.* 46 (2013) 1427–1437.
- [46] D.H. Wang, Y. Yu, H.L. Xin, R. Hovden, P. Ercius, J.A. Mundy, H. Chen, J.H. Richard, D.A. Muller, F.J. DiSalvo, *Nano Lett.* 12 (2012) 5230–5238.
- [47] M. Shao, K. Shoemaker, A. Peles, K. Kaneko, L. Protsailo, *J. Am. Chem. Soc.* 132 (2010) 9253–9255.
- [48] H. Zhu, S. Zhang, S. Guo, D. Su, S. Sun, *J. Am. Chem. Soc.* 135 (2013) 7130–7133.
- [49] R. Mancharan, J.B. Goodenough, *J. Mater. Chem.* 2 (1992) 875–887.
- [50] C. Xu, L. Wang, R. Wang, K. Wang, Y. Zhang, F. Tian, Y. Ding, *Adv. Mater.* 21 (2009) 2165–2169.
- [51] X. Ma, L. Luo, L. Zhu, L. Yu, L. Sheng, K. An, Y. Ando, X. Zhao, *J. Power Sources* 241 (2013) 274–280.
- [52] A.M. Hofstead-Duffy, D.-J. Chen, S.-G. Sun, Y.J. Tong, *J. Mater. Chem.* 22 (2012) 5205–5208.
- [53] G.A. Tritsarlis, J. Rossmeisl, *J. Phys. Chem. C* 116 (2012) 11980–11986.
- [54] I.E.L. Stephens, A.S. Bondarenko, U. Gronbjerg, J. Rossmeisl, I. Chorkendorff, *Energy Environ. Sci.* 5 (2012) 6744–6762.
- [55] C. Xu, Y. Liu, Q. Hao, H. Duan, *J. Mater. Chem. A* 1 (2013) 13542–13548.
- [56] X. Yang, X. Liu, X. Meng, X. Wang, G. Li, C. Shu, L. Jiang, C. Wang, *J. Power Sources* 240 (2013) 536–543.
- [57] J.R. Kitchin, J.K. Nørskov, M.A. Barteau, J.G. Chen, *Phys. Rev. Lett.* 93 (2004) 156801.
- [58] I. Dutta, M.K. Carpenter, M.P. Balogh, J.M. Ziegelbauer, T.E. Moylan, M.H. Atwan, N.P. Irish, *J. Phys. Chem. C* 114 (2010) 16309–16320.
- [59] R. Wang, C. Xu, X. Bi, Y. Ding, *Energy Environ. Sci.* 5 (2012) 5281–5286.
- [60] M. Shao, B.H. Smith, S. Guerrero, L. Protsailo, D. Su, K. Kaneko, J.H. Odell, M.P. Humbert, K. Sasaki, J. Marzullo, R.M. Darling, *Phys. Chem. Chem. Phys.* 15 (2013) 15078–15090.
- [61] S. Guo, S. Zhang, D. Su, S. Sun, *J. Am. Chem. Soc.* 135 (2013) 13879–13884.
- [62] C. Wang, N.M. Markovic, V.R. Stamenkovic, *ACS Catal.* 2 (2012) 891–898.
- [63] J. Wu, H. Yang, *Acc. Chem. Res.* 46 (2013) 1848–1857.
- [64] S. Guo, S. Zhang, S. Sun, *Angew. Chem. Int. Ed.* 52 (2013) 8526–8544.